Received: 25 August 2020 | Revised: 16 February 2021 | Accepted: 17 February 2021 | Published on: 22 March 2021

DOI: 10.1002/qj.4006

Quarterly Journal of the Royal Meteorological Society RMetS

RESEARCH ARTICLE

# A high-accuracy global prognostic model for the simulation of Rossby and gravity wave dynamics

**Sergiy Vasylkevych** | **Nedjeljka Žagar**

Meteorological Institute, Center for Earth System Research and Sustainability, Universität Hamburg, Hamburg, Germany

**Correspondence**
Sergiy Vasylkevych, Meteorological Institute, Universität Hamburg, Grindelberg 7, Hamburg 20144, Germany.
Email: sergiy.vasylkevych@uni-hamburg.de

**Funding information**
UHH Ideen- und Risikofund

**Abstract**

A model for studying Transient Inertia–Gravity And Rossby wave dynamics (TIGAR) is introduced. The presented horizontal component of the model solves the nonlinear rotating shallow-water equations on the sphere using Hough harmonics. Spectral modelling using Hough harmonics as basis functions describes atmospheric dynamics in terms of physically identifiable structures: Rossby and inertia–gravity eigensolutions of linearized primitive equations. This offers an attractive framework for detangling gravity wave dynamics in high-resolution simulations. Accurate computations are achieved through the use of higher order integrating factor and exponential time-differencing methods, leading to a major increase in computational efficiency and stability. A comparison with classical time-stepping schemes shows accuracy improvements of several orders of magnitude at no additional computational cost. In particular, stability gains are achieved through enhanced accuracy and efficiency in the computation of gravity waves, rather than through their damping. In the new framework, reduced models using Rossby and gravity waves aimed at studying dynamical aspects of data assimilation or wave interactions are easily implemented.

**KEYWORDS**

exponential time-stepping schemes, gravity waves, Hough harmonics, nonlinear wave dynamics, numerical model accuracy, Rossby waves

## 1 | INTRODUCTION

Resolving inertia–gravity (IG, or gravity) waves provides an avenue for the improvement of numerical weather prediction (NWP) and climate models (Wedi *et al.*, 2020), but it also poses a challenge for the formulation of numerical schemes, due to the different time-scales of Rossby wave dynamics and faster propagating gravity waves. This imposes severe restrictions on the time step, due to the Courant–Friedrich–Levy (CFL) instability, whenever an explicit time-marching scheme is used. The challenges are not getting smaller, as the models aim at resolving smaller temporal and spatial scales and at reproducing interactions across the observed variability spectrum. The computational costs rise and the validation of numerical schemes becomes increasingly difficult. The challenges escalate in the tropical atmosphere compared with the extratropics, due to the loss of separability between Rossby and IG wave dynamics across scales.

Dynamics, emission, and dissipation of IG waves and their interactions with Rossby waves and the mean flow have been simulated by numerical models of

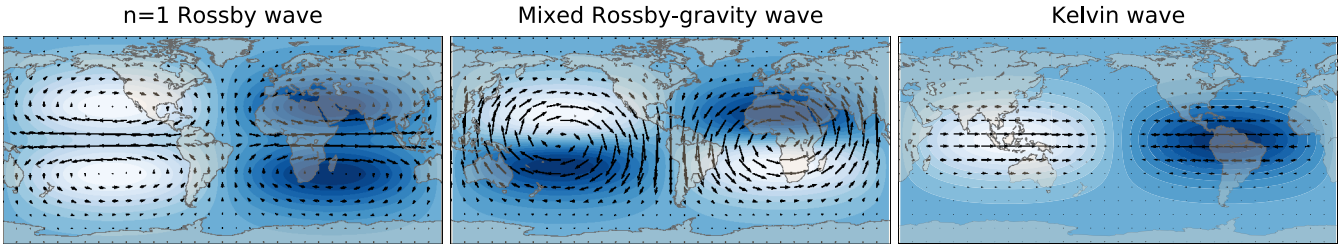


**FIGURE 1** The most studied Hough harmonics: the mixed Rossby–gravity wave, the Rossby mode with meridional mode $n = 1$, and the Kelvin wave, all for fluid depth $D = 1,500$ m and zonal wavenumber $k = 1$. For each mode, the wind components are scaled by the maximal wind. The geopotential height (shades) is scaled by the maximal geopotential [Colour figure can be viewed at wileyonlinelibrary.com]

different complexity (e.g., Kitamura and Matsuda, 2010; Plougonven and Zhang, 2014). Theoretical understanding relies on making simplifications to the governing equations, which leads to reduced models. One way to separate the Rossby and gravity waves is normal-mode function decomposition (e.g., Andrews *et al.*, 1987), where the two dynamical regimes are defined as eigensolutions of the linearized primitive equations on the sphere. The normal-mode approach has been successful for the initialization of NWP models (e.g., Tribbia, 1984; Errico, 1997), for process understanding (e.g., Dörnbrack *et al.*, 2018; Tanaka and Žagar, 2020), and for the diagnosis of models (e.g., Ko *et al.*, 1981) and energy spectra (e.g., Kitamura and Matsuda, 2010; Terasaki *et al.*, 2011; Žagar *et al.*, 2017). It showed that the gravity wave spectrum in high-resolution models follows a power law of $k^{-5/3}$, where $k$ represents the zonal wavenumber. The details of the dynamics behind the $-5/3$ spectrum constitute one of the questions motivating the development of a model that can resolve nonlinear IG and Rossby wave dynamics and their interactions in spectral space explicitly. This article presents the first step towards such a model.

Our motivation for building the Transient Inertia–Gravity And Rossby wave dynamics (TIGAR[1]) model was a desire to study atmospheric dynamics directly in terms of physically identifiable structures such as Rossby and IG waves, rather than going through the intermediate translation process, which is necessary with currently available models. The mathematical foundation for TIGAR is the normal-mode function decomposition, which decouples the primitive prognostic equations for spectral coefficients of Rossby and gravity waves. In the global framework, this is achieved by using the Hough harmonic functions (Longuet-Higgins, 1968) as the expansion functions for discretization of the equations for horizontal motions on the sphere, the nonlinear rotating shallow-water (RSW) equations. The Hough functions are eigenfunctions of the following eigenvalue problem, known as the Laplace tidal equation:

$$\mathcal{F}(\Theta) + \epsilon\Theta = 0, \tag{1}$$

where the linear differential operator $\mathcal{F}$ is defined as

$$\mathcal{F}(\Theta) \equiv \frac{d}{d\mu}\left(\frac{1-\mu^2}{\omega^2-\mu^2}\frac{d\Theta}{d\mu}\right) - \frac{1}{\omega^2-\mu^2}\left[\frac{k}{\omega}\frac{\omega^2+\mu^2}{\omega^2-\mu^2} + \frac{k^2}{1-\mu^2}\right]\Theta, \tag{2}$$

with

$$\mu = \sin\varphi, \quad d\mu = \cos\varphi\, d\varphi, \quad \text{and} \quad \epsilon = \frac{4a^2\Omega^2}{gD}.$$

The quantity $\epsilon$ is referred to as the Lamb parameter. Other parameters are as follows: $\varphi$, $k$, $\omega$, $a$, and $g$ denote the latitude, the zonal wavenumber, the dimensionless wave frequency normalized by the Earth's rotation rate $\Omega$, the Earth's radius, and the acceleration due to the Earth's gravity. The eigenvalue problem in Equation 1 appears in solving the linearized shallow-water equations on the sphere about a basic state of rest and a mean depth $D$, meaning that the Hough functions are eigenmodes of the linearized horizontal motions composed of the Rossby and inertia–gravity modes.

The most studied Hough harmonics are the Rossby wave with the lowest meridional mode and zonal wavenumber 1, shown in Figure 1, and the Kelvin and mixed Rossby–gravity waves, associated with a significant portion of tropical variability. For small $D$, the solutions on the equatorial $\beta$-plane in terms of parabolic cylinder functions do not differ significantly from the spherical solutions (Boyd, 2018).

Physical meaningfulness of the Hough harmonics made them attractive for numerical weather prediction (NWP) and data assimilation early on. For example, they were applied for the first objective analysis at the national

[1]This particular choice of acronym is in line with the Hamburg tradition, as TIGAR follows the suite of models named PUMA and CAT developed by the atmospheric dynamics group at UHH.

weather service in the USA in the 1970s (Flattery, 1970), and were widely used for the initialization of NWP models until the mid-1990s (e.g., Tribbia, 1984; Errico, 1997). More recently, a Hough harmonics based diagnostic of data assimilation systems and NWP models improved understanding of data assimilation, tropical circulations, and practical predictability (Žagar *et al.*, 2015a; 2016a), suggesting the Hough decomposition as a physically meaningful approach to multivariate diagnostics of weather and climate models. The MODES software developed for this purpose (Žagar *et al.*, 2015b) has been applied for real-time monitoring of operational European Centre for Medium-Range Weather Forecasts (ECMWF) forecasts[2] (Žagar *et al.*, 2016b). The Hough harmonics can also be applied for checking the numerical solutions of the discretized shallow-water equations (Dee and Da Silva, 1986). Further usage of Hough harmonics is described in a recent book on applications of normal-mode function decomposition in weather and climate research (Žagar and Tribbia, 2020).

The Hough harmonics, being both waves and orthogonal normal basis functions, are promising basis functions for a prognostic model. In particular, they offer an exciting alternative to spherical harmonics, which are eigensolutions of the global barotropic vorticity equation. The application of Hough harmonics as basis functions for a forecast model was explored in the 1970s by Akira Kasahara at the National Center for Atmospheric Research in the United States (Kasahara, 1977; 1978), and later by Callaghan *et al.* (1999). Kasahara (1977; 1978) presented an integration of the RSW equations using a nondivergent initial condition, a Haurwitz wave with zonal wavenumber 6, and the leap frog time integration scheme for a six-day long forecast. A single test performed by A. Kasahara illustrated potential benefits of the Hough function based discretization compared with spherical harmonics. First, one can investigate interactions between slow-evolving Rossby waves and faster gravity waves. Second, the initialization is simplified greatly, making such a model very suitable for data assimilation research. Furthermore, large-scale modes, derived by linearization about a state of rest, do not differ significantly from the case of realistic zonal winds, and may be computed more accurately.

With the code of earlier models lost and gravity wave dynamics of great interest in weather and climate models approaching the km scale, the revival of the Hough harmonics based dynamical code is a timely effort. Envisaged applications of TIGAR range from wave interactions to data assimilation and predictability studies in 2D and 3D setups. The present study describes the 2D model formulation and time-stepping schemes, which provide high-accuracy solutions needed for research into wave instabilities.

We present a major benefit of the new model, coming from decoupling of the Rossby and gravity modes in the linearized equations, which has not been considered so far. As we show, Hough harmonics as basis functions offer a number of computational advantages, such as fast convergence and remarkable stability without any explicit numerical diffusion applied. The principle reason behind the model performance can be clearly exposed mathematically; it is a cumulative effect of using a time-stepping method with a wide region of stability near the imaginary axis in combination with transformation that reduces the stiffness of the system. Benefits of the selective treatment of different wave types are exposed by employing novel time-stepping methods, the integrating factor (IF) and exponential time-differencing (ETD) schemes (e.g., Boyd, 2001; Kassam and Trefethen, 2005). These are two classes of time-stepping schemes for semilinear ordinary differential equations (ODEs), where a variable change removes stiffness of the problem by integrating the linear dynamics exactly. As we will show, this allows us to raise significantly the upper bound on the time step for explicit algorithms imposed by the CFL stability condition at a trivial computational cost. The results presented complement recent approaches to improve the stability by subtracting the directly solved linear dynamics in a semi-implicit scheme, thereby balancing the initial condition (Benacchio and Klein, 2019), and by resolving the dynamics as a perturbation of an advantageously chosen ambient state (Smolarkiewicz *et al.*, 2019).

The article has the following structure. In Section 2 we introduce the Hough function based spectral model. Section 3 describes the numerical formulation of TIGAR. Significant attention here is given to TIGAR's time-stepping options, in particular the IF and ETD schemes. In Section 4, we present test cases focusing on the barotropic instability, involving both Rossby and gravity wave dynamics. The conclusions and outlook are presented in Section 5.

## 2 | MATHEMATICAL MODEL FORMULATION

2D TIGAR solves rotating shallow-water equations on the sphere. Expressed in spherical coordinates $(\lambda, \varphi) \in [0, 2\pi) \times (-\pi/2, \pi/2)$, they read

$$\frac{du}{dt} - \left(2\Omega \sin\varphi + \frac{u \tan\varphi}{a}\right) v + \frac{g}{a \cos\varphi} \frac{\partial h}{\partial \lambda} = 0, \quad (3a)$$

[2]http://modes.cen.uni-hamburg.de

$$\frac{dv}{dt} + \left(2\Omega \sin\varphi + \frac{u \tan\varphi}{a}\right) u + \frac{g}{a}\frac{\partial h}{\partial \varphi} = 0, \tag{3b}$$

$$\frac{d\,(h - h_s)}{dt} + (h - h_s)\,\nabla \cdot \mathbf{V} = 0, \tag{3c}$$

where $\mathbf{V} = (u, v)$ is the horizontal velocity of the fluid, $h$ is its height above the reference surface (sea level) and $h_s$ is the orography, so that $h - h_s$ is the total depth of the fluid. The material derivative is

$$\frac{d}{dt} = \frac{\partial}{\partial t} + \mathbf{V} \cdot \nabla, \tag{4}$$

and the 2D gradient operator in spherical coordinates is given by $\nabla = (a\cos\varphi)^{-1}\, i\partial/\partial\lambda + a^{-1}\, j\partial/\partial\varphi$.

As a first step, by introducing the mean depth $D$ and rescaling time as $\tilde{t} = 2\Omega t$, Equation 3 is nondimensionalized as

$$\frac{\partial \tilde{u}}{\partial \tilde{t}} - \tilde{v}\sin\varphi + \frac{\gamma}{\cos\varphi}\frac{\partial \tilde{h}}{\partial \lambda} = -\gamma\left(\tilde{\mathbf{V}} \cdot \tilde{\nabla}\tilde{u} - \tilde{u}\,\tilde{v}\,\tan\varphi\right) \equiv N_u, \tag{5a}$$

$$\frac{\partial \tilde{v}}{\partial \tilde{t}} + \tilde{u}\,\sin\varphi + \gamma\,\frac{\partial \tilde{h}}{\partial \varphi} = -\gamma\left(\tilde{\mathbf{V}} \cdot \tilde{\nabla}\tilde{u} + \tilde{u}^2 \tan\varphi\right) \equiv N_v, \tag{5b}$$

$$\frac{\partial \tilde{h}}{\partial \tilde{t}} + \gamma\,\tilde{\nabla} \cdot \tilde{\mathbf{V}} = -\gamma\left(\tilde{\mathbf{V}} \cdot \tilde{\nabla}(\tilde{h} - \tilde{h}_s) + (\tilde{h} - \tilde{h}_s)\tilde{\nabla} \cdot \tilde{\mathbf{V}}\right) \equiv N_h, \tag{5c}$$

where $\gamma$ is defined as

$$\gamma = \frac{\sqrt{gD}}{2a\Omega} = \epsilon^{-1/2},$$

$\tilde{\mathbf{V}} = (\tilde{u}, \tilde{v})$ and $\tilde{\nabla} = a\nabla$ are the nondimensional horizontal velocity and del operator, respectively, and

$$u = \tilde{u}\sqrt{gD}, \quad v = \tilde{v}\sqrt{gD}, \quad h = D(\tilde{h} + 1), \quad h_s = D\tilde{h}_s. \tag{6}$$

We remark that Equation 5 is also the form in which RSW equations appear in the normal mode-function decomposition of the primitive equations. In that case, the equivalent depth $D > 0$ is obtained as a solution of vertical structure equations (e.g., Kasahara and Puri, 1981).

The linearization of RSW, obtained by setting the right-hand side of Equation 5 to zero, yields Laplace tidal equations without the tide-generating force. As discussed in Kasahara (1977; 2020), the wave solutions of the Laplace tidal equation give rise to an orthonormal basis in $L^2$ on the sphere, which enables the concept of the Hough spectral model. Specifically, there exists a set of fields

$$\mathbf{H}^k_{n,l}(\lambda, \varphi) = \mathbf{\Theta}^k_{n,l}(\varphi) e^{ik\lambda}, \tag{7a}$$

where $k, n$ stand for the zonal and meridional wavenumber indices, respectively, and $l = 1, 2, 3$ indicates the type of the wave, such that the set $\{\mathbf{H}^k_{n,l} \mid |k| = 0, 1, \ldots; n = 0, 1, \ldots; l = 1, 2, 3\}$ is an orthonormal basis of $L^2$ on the sphere and

$$\left(\tilde{u}^k_{n,l}, \tilde{v}^k_{n,l}, \tilde{h}^k_{n,l}\right)^{\mathrm{T}} = e^{-i\omega^k_{n,l}\tilde{t}}\,\mathbf{H}^k_{n,l} \tag{7b}$$

is a solution of Equation 5 with nonlinearity $\mathbf{N} = (N_u, N_v, N_h)^{\mathrm{T}} = 0$. Following Swarztrauber and Kasahara (1985), we will refer to $\mathbf{H}^k_{n,l}$ and $\mathbf{\Theta}^k_{n,l}$ as Hough harmonics and Hough functions, respectively. The three wave types denoted by $l = 1, 2, 3$ are eastward-propagating inertia–gravity (EIG), westward-propagating inertia–gravity (WIG), and Rossby waves, respectively. The two kind of normal modes, IG and Rossby waves, are traditionally known as solutions of the first and second kind, respectively, of the linearized primitive equations (Longuet-Higgins, 1968). The three components of the Hough function vector $\mathbf{\Theta}^k_{n,l}$,

$$\mathbf{\Theta}^k_{n,l}(\varphi) = \begin{vmatrix} U^k_{n,l}(\varphi) \\ iV^k_{n,l}(\varphi) \\ Z^k_{n,l}(\varphi) \end{vmatrix}, \tag{8}$$

describe the meridional eigenstructure of the zonal velocity $U$, meridional velocity $V$, and geopotential height $Z$ fields. The imaginary unit factor $i$ in front of $V$ accounts for the phase shift of $\pi/2$ with respect to $U$. The Hough functions $\mathbf{\Theta}^k_{n,l}$ and corresponding frequencies $\omega^k_{n,l}$ are computed using spherical harmonic expansion; the applied algorithm was developed by Swarztrauber and Kasahara (1985). Given the equivalent depth $D$ for each zonal wavenumber $k$, the frequencies $\omega^k_{n,l}$ of the Hough functions are obtained as the eigenvalues. This method differs from the original eigenvalue problem for tidal waves, where the wave frequencies and zonal wavenumber are specified and equivalent depths are obtained as eigenvalues. Details on the Hough harmonics computation in terms of Legendre polynomials can be found in Swarztrauber and Kasahara (1985) and Kasahara (2020); other methods are presented in Wang *et al.* (2016). Kasahara (2020) also provides details of his prognostic model based on the Hough basis functions. TIGAR is built on the same equation set.

Normalized frequencies of the Rossby and gravity modes for a single value of $D$ are shown in Figure 2. Given $n$, each curve connects discrete frequencies for a range of zonal wavenumbers. Two special solutions filling the frequency gap between slow Rossby modes and fast IG modes are the mixed Rossby–gravity (MRG) wave and Kelvin wave. Throughout the article, the MRG wave and Kelvin wave are counted as part of the Rossby and EIG modes,

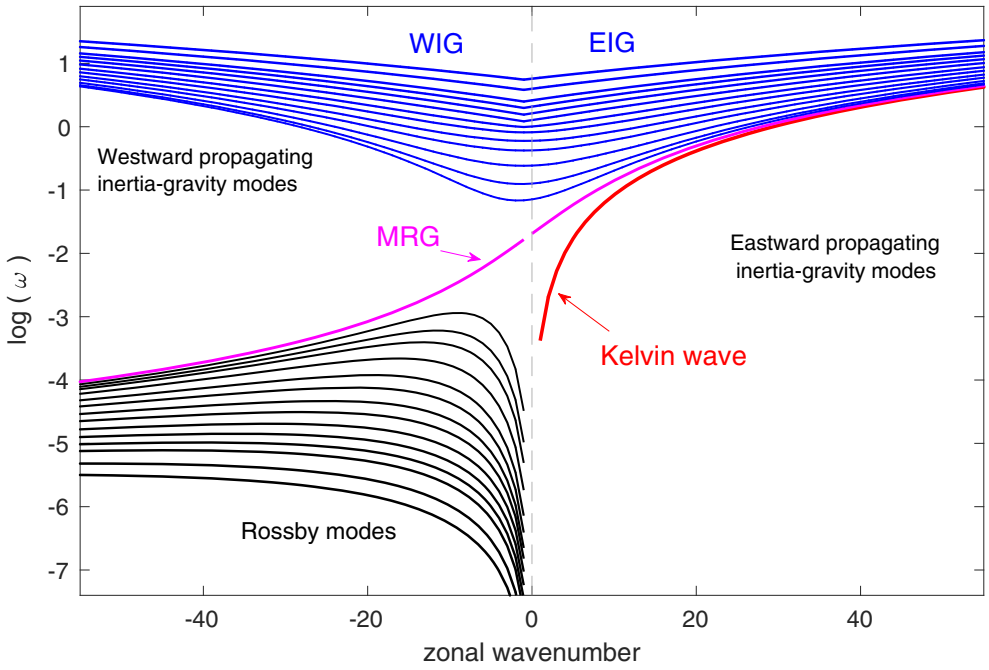


**FIGURE 2** Dispersion curves of the linear wave solutions of the global shallow-water equations linearized around the state of rest for $D = 100$ m. WIG and EIG denote the westward-propagating and eastward-propagating inertia-gravity modes, respectively, whereas MRG stands for the mixed Rossby–gravity wave. Frequency is normalized by $2\Omega$. The dispersion curves for the 14 lowest meridional modes for each wave type are shown [Colour figure can be viewed at wileyonlinelibrary.com]

respectively, as suggested by Figure 2. Examples of Hough functions are shown in Figure 1. As $D$ decreases, the frequency gap between the IG and Rossby modes at large scales reduces and the dispersion curves of the Kelvin and MRG waves become more distinct from other large-scale waves (see, e.g., the figures in Žagar *et al.*, 2015b).

The case $k = 0$, representing the zonal mean state, is special. Two sets of orthonormal Rossby modes, corresponding to the geostrophic steady states, are known. Kasahara (1978) constructed the set of K-modes from Legendre polynomials, while Shigehisa (1983) obtained the so-called S-modes as a $k \to 0$ limit of the Rossby solution of the Laplace tidal equations. A comparison conducted by Tanaka and Kasahara (1992) showed that K-modes provide faster convergence, while S-modes have more similarities with nonzonal rotational modes. We used exclusively $K$-modes for all the modelling discussed in the article. As seen in Figure 2, frequencies for $k = 0$ Rossby modes are all zero.

Since Hough harmonics form a basis, an arbitrary solution of the RSW Equation 5 can be expressed as

$$\left(\tilde{u}, \tilde{v}, \tilde{h}\right)^{\mathrm{T}} = \sum_{k,n,l} W^k_{n,l}(t)\ \mathbf{H}^k_{n,l}. \tag{9}$$

Exploiting the orthogonality of Hough harmonics over the sphere, it follows that Equation 5 is equivalent to the spectral problem

$$\frac{dW^k_{n,l}(\tilde{t})}{d\tilde{t}} + i\omega^k_{n,l} W^k_{n,l}(\tilde{t}) = f^k_{n,l}(\tilde{t}), \tag{10a}$$

with

$$f^k_{n,l} = \frac{1}{2\pi}\int_0^{2\pi}\int_{-1}^{1} \mathbf{N}\left(\sum_{k',n',l'} W^{k'}_{n',l'}\mathbf{H}^{k'}_{n',l'}\right) \cdot \left(\mathbf{H}^k_{n,l}\right)^*(\lambda,\mu)\ d\mu\ d\lambda. \tag{10b}$$

In summary, the Hough-function decomposition, which expands the wind and height fields over the basis consisting of eigenmodes of the linear rotating shallow-water equations on the sphere, transforms the nonlinear RSW Equation 3 into the spectral ODE

$$\dot{\mathbf{W}} + i\mathbb{L}\mathbf{W} = f(\mathbf{W}), \tag{11}$$

where $\mathbf{W}$ is a complex vector with the Hough expansion coefficients, $i\mathbb{L}$ is a skew-adjoint operator given by eigenfrequencies $\omega_1, \ldots, \omega_N$ of RSW, $\mathbb{L} = \mathrm{diag}(\omega_1, \ldots, \omega_N)$, and $f$ is a quadratic function induced by RSW nonlinearity, with elements $f^k_{n,l}$ defined by Equation 10b.

In order to solve Equation 11, the initial values (time-step 0) of velocity and height fields must be rescaled according to Equation 6 and projected on to Hough harmonics to determine the initial values of spectral coefficients via

$$W^k_{n,l}(0) = \frac{1}{2\pi}\int_0^{2\pi}\int_{-1}^{1} \mathbf{X}_0 \cdot \left(\mathbf{H}^k_{n,l}\right)^*(\lambda,\mu)\ d\mu\ d\lambda, \tag{12}$$

where $\mathbf{X}_0 = \left(\tilde{u}_0, \tilde{v}_0, \tilde{h}_0\right)^{\mathrm{T}}$ is the vector of the initial normalized winds and geopotential height. The evolution of spectral coefficients is computed

by solving the ordinary differential Equation 10, while the corresponding values of velocity and height fields are reconstructed from Equations 9 and 6.

## 3 | NUMERICAL FORMULATION OF TIGAR

The numerical code of TIGAR builds upon the MODES software described in Žagar *et al.* (2015b). From MODES, TIGAR borrows the grid-generation utility, data structure, computation of Hough functions, their derivatives and frequencies $\omega^k_{n,l}$, and routines for the zonal expansion using fast Fourier transform (FFT), and for the Hough function projection. The computation of Hough functions is a relatively time-consuming task, but they are computed only once for each model setup and saved for repeated use. As seen from Equations 7 and 10, the horizontal velocity and geopotential height can be reconstructed from spectral coefficients provided the Hough functions $\mathbf{\Theta}^k_{n,l}$ and corresponding frequencies $\omega^k_{n,l}$ are known. Computations are performed on a regular Gaussian grid, with the optimal ratio between the number of meridional modes and zonal waves determined by truncation, as explained below.

### 3.1 | Evaluation of nonlinear terms

The contributions of nonlinear terms are computed pseudospectrally. To this end, the fields are transformed to the physical grid, where the nonlinear terms are evaluated. The result is then transformed to modal space via FFT in the zonal direction followed by Hough-function decomposition in the meridional direction. This strategy is facilitated by the fact that Hough functions, together with their derivatives, can be computed with machine precision from Legendre polynomials, and then both can be stored for repeated use.

The nonlinear terms on the right-hand side of Equation 5 can be evaluated in multiple ways, which are equivalent analytically, despite the difference in computational procedures. Three such possibilities are discussed in Temperton (1991). In Swarztrauber (1981) (see also the discussion in Browning *et al.*, 1989), it was shown that computing the nonlinear terms as

$$N_u = \gamma\left[\tilde{u}\left(\frac{\partial\tilde{v}}{\partial\varphi} - \tilde{\delta}\right) - \tilde{v}\frac{\partial\tilde{u}}{\partial\varphi}\right], \tag{13a}$$

$$N_v = -\gamma\left[\tilde{u}\left(\frac{\partial\tilde{u}}{\partial\varphi} + \tilde{\xi}\right) - \tilde{v}\frac{\partial\tilde{v}}{\partial\varphi}\right], \tag{13b}$$

$$N_h = -\gamma\left[\frac{\tilde{u}}{\cos\varphi}\frac{\partial(\tilde{h}-\tilde{h}_s)}{\partial\lambda} + \tilde{v}\frac{\partial(\tilde{h}-\tilde{h}_s)}{\partial\varphi} + \tilde{\delta}(\tilde{h}-\tilde{h}_s)\right], \tag{13c}$$

where $\tilde{\xi} = (\partial\tilde{v}/\partial\lambda - \partial(\tilde{u}\cos\varphi)/\partial\varphi)/\cos\varphi$ and $\tilde{\delta} \equiv \tilde{\nabla}\cdot\tilde{\mathbf{V}} = (\partial\tilde{u}/\partial\lambda + \partial(\tilde{v}\cos\varphi))/\cos\varphi$ stand for the nondimensional relative vorticity and divergence, respectively, involves evaluation of bounded expressions only and thus avoids potential problems with discontinuity at the poles. This vorticity-divergence formulation is used by many spectral models (e.g., Hoskins and Simmons, 1988; Fraedrich *et al.*, 2009). Vorticity, divergence, and partial derivatives in grid-point space are reconstructed from spectral coefficients $W^k_{n,l}$ and stored meridional profiles $\hat{\xi}^k_{n,l}(\varphi)$, $\hat{\delta}^k_{n,l}(\varphi)$, and $\partial\mathbf{\Theta}^k_{n,l}(\varphi)/\partial\varphi$, in the same manner as for wind and height fields. The equations read as

$$\tilde{\xi} = \sum_{k,n,l} e^{ik\lambda} W^k_{n,l}\,\hat{\xi}^k_{n,l}, \quad \tilde{\delta} = \sum_{k,n,l} e^{ik\lambda} W^k_{n,l}\,\hat{\delta}^k_{n,l} e^{ik\lambda}, \tag{14a}$$

$$\left[\frac{\partial\tilde{u}}{\partial\varphi}, \frac{\partial\tilde{v}}{\partial\varphi}, \frac{\partial\tilde{h}}{\partial\varphi}\right]^{\mathrm{T}} = \sum_{k,n,l} e^{ik\lambda} W^k_{n,l}\,\frac{\partial\mathbf{\Theta}^k_{n,l}}{\partial\varphi}, \tag{14b}$$

$$\left[\frac{\partial\tilde{u}}{\partial\lambda}, \frac{\partial\tilde{v}}{\partial\lambda}, \frac{\partial\tilde{h}}{\partial\lambda}\right]^{\mathrm{T}} = \sum_{k,n,l} e^{ik\lambda} W^k_{n,l}\, ik\,\mathbf{\Theta}^k_{n,l}. \tag{14c}$$

An alternative way to achieve the same goal is to rewrite the nonlinearity in terms of differentials of $\mathcal{U}$ and $\mathcal{V}$, where

$$\mathcal{U} = \tilde{u}\,\cos\varphi, \quad \mathcal{V} = \tilde{v}\cos\varphi, \tag{15}$$

so that

$$N_u = -\frac{\gamma}{\cos\varphi}\left[\tilde{u}\frac{\partial\tilde{u}}{\partial\lambda} + \tilde{v}\frac{\partial\mathcal{U}}{\partial\varphi}\right], \tag{16a}$$

$$N_v = -\frac{\gamma}{\cos\varphi}\left[\tilde{u}\frac{\partial\tilde{v}}{\partial\lambda} + \tilde{v}\frac{\partial\mathcal{V}}{\partial\varphi}\right] - \gamma(\tilde{u}^2+\tilde{v}^2)\tan\varphi, \tag{16b}$$

$$N_h = -\gamma\left[\frac{\tilde{u}}{\cos\varphi}\frac{\partial(\tilde{h}-\tilde{h}_s)}{\partial\lambda} + \tilde{v}\frac{\partial(\tilde{h}-\tilde{h}_s)}{\partial\varphi} + \frac{\tilde{h}-\tilde{h}_s}{\cos\varphi}\left(\frac{\partial\tilde{u}}{\partial\lambda} + \frac{\partial\mathcal{V}}{\partial\varphi}\right)\right]. \tag{16c}$$

This approach is analogous to the $U-V$ formulation due to Ritchie (1988) (see also Temperton, 1991, and references therein). As before, the partial derivatives in grid-point space are reconstructed from spectral coefficients using Equation 14. The stored profiles for derivatives should now include $\partial\left(\mathbf{\Theta}^k_{n,l}\cos\varphi\right)/\partial\varphi$ for the wind components. Both of the above methods were implemented and tested. Neither of the methods was found preferable and, for the

sake of consistency, all the simulations presented were performed using the $U - V$ formulation.

### 3.2 | Grid, resolution, and spectral truncation

TIGAR uses a regular Gaussian grid $N_\lambda \times N_\varphi$, where $N_\varphi$ is the total number of latitude circles. Two spectral truncation schemes are implemented: parallelogram (which includes rhomboidal) and triangular. In the parallelogram truncation, denoted $P_{K\times N}$, the numbers of zonal and meridional waves retained in the Hough spectral expansion, Equation 9, are independent of each other, so that

$$(\tilde{u}, \tilde{v}, \tilde{h})^{\mathrm{T}} = \sum_{|k|\le K} \sum_{n=0}^{N} \sum_{l=1}^{3} W^k_{n,l}(t)\, \mathbf{H}^k_{n,l}. \tag{17}$$

The rhomboidal truncation $R_K$, which was dominant in spectral NWP systems until the second part of the 1970s, is a particular case of parallelogram truncation with $N = K$.

For the triangular truncation, denoted $T_K$, the number of Hough functions retained in the expansion decreases with zonal wavenumber, so that

$$(\tilde{u}, \tilde{v}, \tilde{h})^{\mathrm{T}} = \sum_{|k|\le K} \sum_{l=1}^{3} \sum_{n=0}^{K-|k|} W^k_{n,l}(t)\, \mathbf{H}^k_{n,l}. \tag{18}$$

Since any Hough function $\mathbf{\Theta}^k_{n,l}$ can be expressed in terms of the Legendre polynomials $P^k_n$ and vice versa (see Swarztrauber and Kasahara, 1985), the resolution of any truncation in the Hough-function model is the same as in a conventional spectral model in spherical harmonics. The triangular truncation, which is the only type used in modern spectral NWP systems, offers a number of theoretical advantages, such as a uniform resolution across the globe and preservation of horizontal isotropy with respect to scaling. To facilitate direct comparison with other spectral models, all simulations presented here are performed with triangular truncation.

For any given truncation, there is an optimal grid, which is the minimal one with an even number of points along each meridian that ensures that nonlinear terms in Equation 10b can be evaluated exactly via FFT and Gaussian quadrature from the grid-point values of Hough functions. For triangular truncation $T_K$, the optimal grid is the canonical regular Gaussian grid $4M \times 2M$, where $M(K)$ is the minimal integer satisfying $M \ge 3K/4$. We refer the reader to Satoh (2013) for details. The optimal grid in the above sense is often called the quadratic grid.

All simulations in this article at $T_{42}$, $T_{85}$, and $T_{170}$ resolutions are performed on optimal grids, while $T_{21}$ and $T_{120}$ runs used finer than optimal $128 \times 64$ and $512 \times 256$ spatial resolutions, respectively.

### 3.3 | Numerical dissipation

In order to prevent energy cascade to the smallest resolvable scales, geophysical fluid dynamics models add artificial dissipative terms to the equations of motion, most often in the form of hyperdiffusion. TIGAR implements such dissipation as a switchable option in the form of spectral viscosity, proposed by Gelb and Gleeson (2001). In his integration of a Haurwitz wave with zonal wavenumber 6 using the leap frog scheme, Kasahara (1978) noticed an excessive growth of amplitudes in higher meridional modes. However, all the experiments in this article are performed with spectral viscosity switched off, suggesting that the applied time-stepping required no explicit damping of small scales.

### 3.4 | Time-stepping schemes

Due to large differences in phase speeds between Rossby and IG modes, the spectral Equation 11 is necessarily stiff, which is a manifestation of the CFL principle. The development of the time-stepping scheme for TIGAR focuses on the benefits of employing two types of algorithms, the integrating factor and exponential time differencing. As we will show, these schemes benefit significantly from the structure of the spectral ODE using the Hough harmonics.

#### 3.4.1 | The integrating factor and exponential time-differencing methods

The integrating factor (IF) and exponential time-differencing (ETD) methods are two classes of time-stepping schemes for semilinear ODEs,

$$\dot{\mathbf{W}} + A\mathbf{W} = f(t, \mathbf{W}), \tag{19}$$

where the linear part of the equation is stiff and the nonlinear part is nonstiff. A concise survey of numerical methods for semilinear stiff partial differential equations (PDEs) can be found in Kassam and Trefethen (2005).

Integrating factor methods were introduced by Lawson (1967), who proposed an IF modification of a classical fourth-order Runge–Kutta scheme (RK4) and compared it with the underlying method. Lawson's algorithm is sometimes referred to as "Lawson 4" in the literature. The underlying idea behind the IF method is to remove

stiffness by integrating the linear dynamics exactly. Introducing a variable change $\mathbf{Y}(t) = e^{tA}\mathbf{W}(t)$, Equation 19 is transformed into

$$\dot{\mathbf{Y}} = e^{tA} f(e^{-tA}\mathbf{Y}). \tag{20}$$

Now applying any classical time-stepping scheme to Equation 20 and reformulating the result in terms of original variable $\mathbf{W}$ will yield an IF variant of the said scheme.

The amplitudes of fast modes can be an order of magnitude or more smaller than those of slow ones, especially outside the Tropics. Thus, discarding the terms quadratic in $\mathbf{W}_f$, Equation 20 can be approximated by

$$\dot{\mathbf{Y}} = e^{tA} f(\mathbf{W}_\mathrm{s}) + e^{tA} Df(\mathbf{W}_\mathrm{s}) e^{-tA}\mathbf{Y}, \tag{21}$$

where $\mathbf{W}_\mathrm{s}$ and $\mathbf{W}_f$ are the projections of $\mathbf{W}$ on slow and fast modes, respectively, and $Df$ is the tangent linear of $f$. The dynamics of the system in Equation 21 is determined by eigenvalues of $Df(\mathbf{W}_\mathrm{s})$. For this reason, as long as $Df(\mathbf{W}_\mathrm{s})$ is not stiff, an explicit method with a large time step can produce a very accurate forecast.

A discussion of advantages and pitfalls of employing IF-type methods in geophysical fluid dynamics can be found in Boyd (2001). Two main concerns connected with their use are the fact that they do not preserve the steady states of the original system (Equation 19) and that they have rather large error constants. The latter issue is captured in the concept of stiff order. A method is said to be of stiff order $p$ whenever its global error over a finite time interval can be uniformly bounded by $C(\Delta t)^p$, where $C$ is a constant that depends on the length of the time interval and on the chosen class of problems, but on neither the stiffness nor the step size $\Delta t$. The stiff-order conditions were derived in Hochbruck and Ostermann (2010). It turns out that high-order IF methods, such as Lawson 4, are only of stiff order 1. In a particular application, the performance of an integration scheme can lie anywhere between its stiff and classical order. Using a method of higher stiff order will have large positive impact on the modeling of gravity waves, thus leading to a better forecast.

Exponential time-differencing schemes rely on the same idea as IF methods, while addressing their shortcomings. Equation 19 is rewritten in integral form as

$$\mathbf{W}(t+\Delta t) = e^{-\Delta t A}\,\mathbf{W}(t) + \int_0^{\Delta t} e^{(t-\tau)A} f(t+\tau, \mathbf{W}(t+\tau))\, d\tau. \tag{22}$$

Now, approximating the nonlinearity, but not the exponent, in Equation 22 by a polynomial in $t$ and integrating the resulting expression exactly yields an ETD scheme. The polynomial approximation may be computed using previous steps of the integration process, resulting in exponential multistep methods, or by Runge–Kutta stages, leading to ETD Runge–Kutta algorithms.

An overview of exponential methods can be found in Minchev and Wright (2005). They were first introduced by Certaine (1960) and Nørsett (1969) and later rediscovered by Cox and Matthews (2002). Reports on the relative merits of IF and ETD methods for Hamiltonian systems vary. While in Kassam and Trefethen (2005) an exponential variant of RK4 due to Cox and Matthews (2002), ETD4RK, proves to be superior to Lawson 4, Berland *et al.* (2006) report more nuanced performance in the context of the nonlinear Schrödinger equation.

The integrating factor and exponential time-differencing methods are currently not used in operational NWP systems, where semi-implicit semi-Lagrangian methods are dominant (e.g., Mengaldo *et al.*, 2019). Clancy and Pudykiewicz (2013) and Gaudreault and Pudykiewicz (2016) investigated the use of exponential integrators proposed by Tokman (2006) in a rotating shallow-water model. Their tests confirm the very good accuracy and stability of exponential integrators, but at a severe computational cost. In the context of RSW on a double periodic domain, Peixoto and Schreiber (2019) compared, among others, the exponential Runge–Kutta method with the state-of-the-art semi-implicit semi-Lagrangian scheme used in ECMWF's Integrated Forecasting System (IFS). RK2E performed on par with the semi-Lagrangian scheme in terms of accuracy and efficiency, but was inferior in stability.

While there is a vast body of evidence regarding the benefits of IF and exponential methods in terms of stability and accuracy in varied physical contexts (Kassam and Trefethen, 2005; Minchev and Wright, 2005; Clancy and Pudykiewicz, 2013; Gaudreault and Pudykiewicz, 2016; Coudiére *et al.*, 2018; Peixoto and Schreiber, 2019), their practical application is hampered by the expense of computing the matrix exponents. For exponential integrators, this problem is compounded by the necessity to evaluate matrix functions:

$$\psi_i(\Delta t A), \quad \text{where} \quad \psi_1(z) = \frac{e^z - 1}{z} \quad \text{and}$$
$$z\psi_{i+1}(z) = \psi_i(z) - \frac{1}{i!}. \tag{23}$$

However, for the RSW model in Hough harmonics, these difficulties disappear, since $A = i\mathbb{L}$ is a diagonal matrix and the exponents are trivial to compute.

### 3.4.2 | Implementation of time-stepping schemes in TIGAR

In TIGAR we have implemented nine time-stepping options, all of which are explicit schemes. We have chosen

three classical methods: fourth-order Runge–Kutta (RK4), third-order Adams–Bashforth, and leapfrog scheme with Robert–Asselin filter, which have relatively large stability domains in the critical neighborhood and which have been widely used in simple and intermediate complexity geophysical models. To evaluate the performance of the IF and ETD methods, we compare the classical fourth-order Runge–Kutta (RK4) and Adams–Bashforth methods with their exponential and integrating factor modifications. To gauge the performance against cheaper lower-order alternatives, we also implemented second- and third-order ETD Runge–Kutta methods proposed by Cox and Matthews (2002).

While testing encompassed all listed time-stepping schemes, here the presentation is restricted to the comparison of RK4 and its IF and ETD derivatives, which incidentally are the best-performing methods of their respective types. It is important to note that, thanks to the diagonal structure of the matrix $\mathbb{L}$, the computational cost per time step of IF and ETD variants is either identical or nearly identical to that of their underlying classical method.

In the interest of clarity and uniformity, throughout this article we will apply a naming convention, where appending a letter "E" or "I" to the abbreviation of a classical method indicates its ETD or IF variant, respectively. Thus, Cox and Matthews (2002) ETD4RK is referred to as RK4E, while Lawson 4 will be denoted as RK4I.

## 4 | NUMERICAL EXPERIMENTS

Four types of analytical solutions of RSW on the sphere are known: global geostrophic steady-state zonal flow, steady zonal jet, solid-body rotation, and zonal jet superimposed on solid-body rotation. The first two are the steady-state solutions and parts of the test suit proposed by Williamson *et al.* (1992), while the latter two are time-dependent flows proposed in Läuter *et al.* (2005). All four tests have been carried out, but we limit the presentation here to one steady-state and one rotating solution. This is followed by the barotropic instability test described in Galewsky *et al.* (2004) as a more interesting simulation for a model aiming at accurate computations of interactions in multiscale flows.

As can be seen from Equations 5 and 10, the magnitude of nonlinear terms in the computational formulation scales as $\sqrt{D}$. Since IF and exponential methods integrate the nonlinear terms exactly, we perform the tests with a large equivalent depth of 10 km, corresponding to the barotropic mode, and $\gamma = 0.337$, where the nonlinear tendencies are the strongest, as it provides the most challenging setting for those methods. For smaller equivalent depths, the computations with these methods can be carried out with even larger time steps and their accuracy and stability advantages over conventional algorithms are even more pronounced.

To represent the error dynamics, we use the standard norms,

$$\|Z\|_{L^p} = \left[\frac{1}{4\pi}\int_0^{2\pi}\int_{-\pi/2}^{\pi_2} |Z(\lambda,\varphi)|^p \cos\varphi \, d\lambda \, d\varphi\right]^{1/p} \quad \text{for } 1 \le p < \infty, \tag{24a}$$

$$\|Z\|_{L^\infty} = \sup_{\lambda,\varphi} |Z(\lambda,\varphi)|, \tag{24b}$$

for arbitrary scalar field $Z$. The errors over the whole integration interval $0 \le t \le T$ are measured in integral norms,

$$\|Z\|_{L^p_T} = \left[\frac{1}{T}\int_0^T \|Z(t)\|^p_{L^p} \, dt\right]^{1/p} \quad \text{for } 1 \le p < \infty, \tag{25a}$$

$$\|Z\|_{L^\infty} = \sup_{0\le t\le T} \|Z(t)\|_{L^\infty}. \tag{25b}$$

For a given reference field $Z_{\text{ref}}$ and a chosen norm $X$, the absolute and relative errors are, respectively, defined as

$$E^{\text{abs}}_X = \|Z - Z_{\text{ref}}\|_X, \quad E^{\text{rel}}_X = \frac{\|Z - Z_{\text{ref}}\|_X}{\|Z_{\text{ref}}\|_X}. \tag{26}$$

Ideally, objective efficiency comparisons between different algorithms should be made at an equal computation time rather than an equal time step. However, since in the Hough framework RK4, RK4I, and RK4E are equally expensive, comparing these methods at an equal time step does provide an efficiency measure.

### 4.1 | Global geostrophic steady-state zonal flow

This is test case 2 of Williamson *et al.* (1992), with the steady-state solution given by

$$u = u_0 \cos\varphi, \quad v = 0, \quad h = h_0 - h_0 \sin^2\varphi,$$
$$h_0 = \frac{1}{g}\left(a\Omega u_0 + \frac{u_0^2}{2}\right). \tag{27}$$

We carry out the simulation using the initial conditions of Equation 27 and $u_0 = 2\pi a/(12 \text{ days})$ for five days. In this test, the spatial discretization errors dominate over time discretization ones and, for conventional time-marching schemes, convergence depends weakly on the time step used. All algorithms converge to machine precision (i.e., to a maximum accuracy of $10^{-15}$). Figure 3 shows the

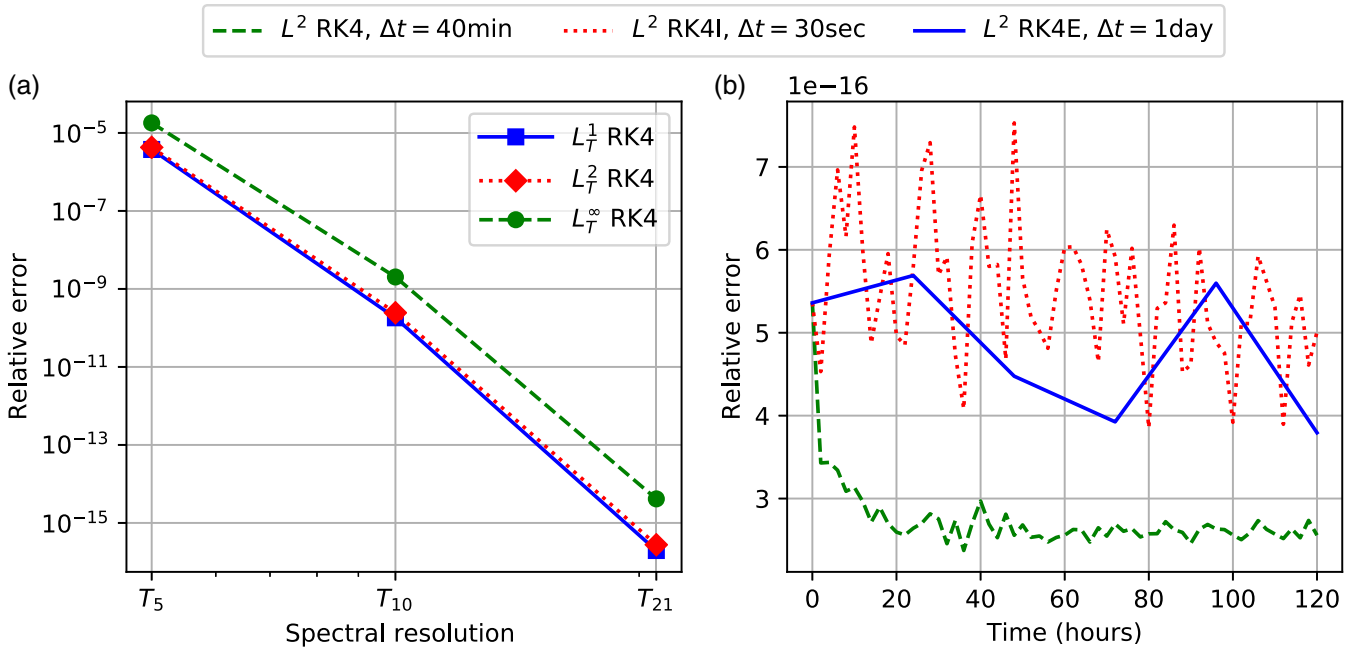


**FIGURE 3** Global steady-state test case convergence results. (a) Relative errors in height field as a function of spectral resolution for RK4 method with time step $\Delta t = 40$ min. (b) Evolution of relative error in height field for converged solutions computed with different time integrators at T21 resolution [Colour figure can be viewed at wileyonlinelibrary.com]

relative errors for converged solutions, together with the time-step at which the convergence occurs. Among different methods, the clear winner is the exponential method, with a ridiculous one-day time step. Clearly worst is the integrating-factor method, which requires a small step size to converge within machine precision. This behaviour, however, is hardly unexpected, as a steady state for Equation 11 is no longer steady for Equation 21. Thus, it represent a dynamic rather than a balance problem for IF methods, making the dependence of accuracy on step size inevitable. For NWP applications, this drawback of IF methods is insignificant, as the errors remain small when simulations are performed with much larger step sizes than shown in Figure 3. For instance, with $\Delta t = 40$ min step size, at the end of day 5 RK4I produces a relative $L^2$ error of $8.5 \times 10^{-8}$.

## 4.2 | Solid body rotation

The analytical solution, presented by Läuter *et al.* (2005), describes the stationary flow in the fixed reference frame, thus rotating clockwise with constant angular velocity $\Omega$ in a coordinate system that rotates with Earth. It requires zonally symmetric orography forcing,

$$h_s = \frac{a\Omega \sin^2 \phi}{2g}. \tag{28}$$

With orography given by Equation 28, balanced velocity and geopotential fields are given as

$$u = u_0(\sin\alpha \sin\phi(\cos\lambda \cos\Omega t - \sin\lambda \sin\Omega t) + \cos\alpha \cos\phi), \tag{29a}$$

$$v = -u_0 \sin\alpha(\sin\lambda \cos\Omega t + \cos\lambda \sin\Omega t), \tag{29b}$$

$$gh = -\frac{1}{2}[u_0(\sin\alpha \cos\phi(-\cos\lambda \cos\Omega t + \sin\lambda \sin\Omega t) + \cos\alpha \sin\phi) + a\Omega \sin\phi\,]^2 + \frac{1}{2}(a\Omega \sin\phi)^2 + k_1, \tag{29c}$$

and they are the solution of the RSW Equation 3. We use the following values of the constant parameters recommended by Läuter *et al.* (2005): $\alpha = \pi/4$, $u_0 = 2\pi a/12$ m · day$^{-1}$ $\approx$ 38.6 m·s$^{-1}$, $k_1 = 133{,}681$ m·s$^{-2}$. Similarly to the global steady state, this test does not require a fine spatial or spectral resolution. Nevertheless, it is a good complementary test verifying the correct functioning of time-stepping schemes and comparing their accuracy.

The results of five-day simulations at T42 resolution are presented in Figure 4. The left panel shows relative errors in the height field as a function of time step. All methods tested demonstrate fourth-order convergence, consistent with their classical numerical order. The best performer again is the exponential integrator scheme, which provides both stability and accuracy unmatched by other methods.

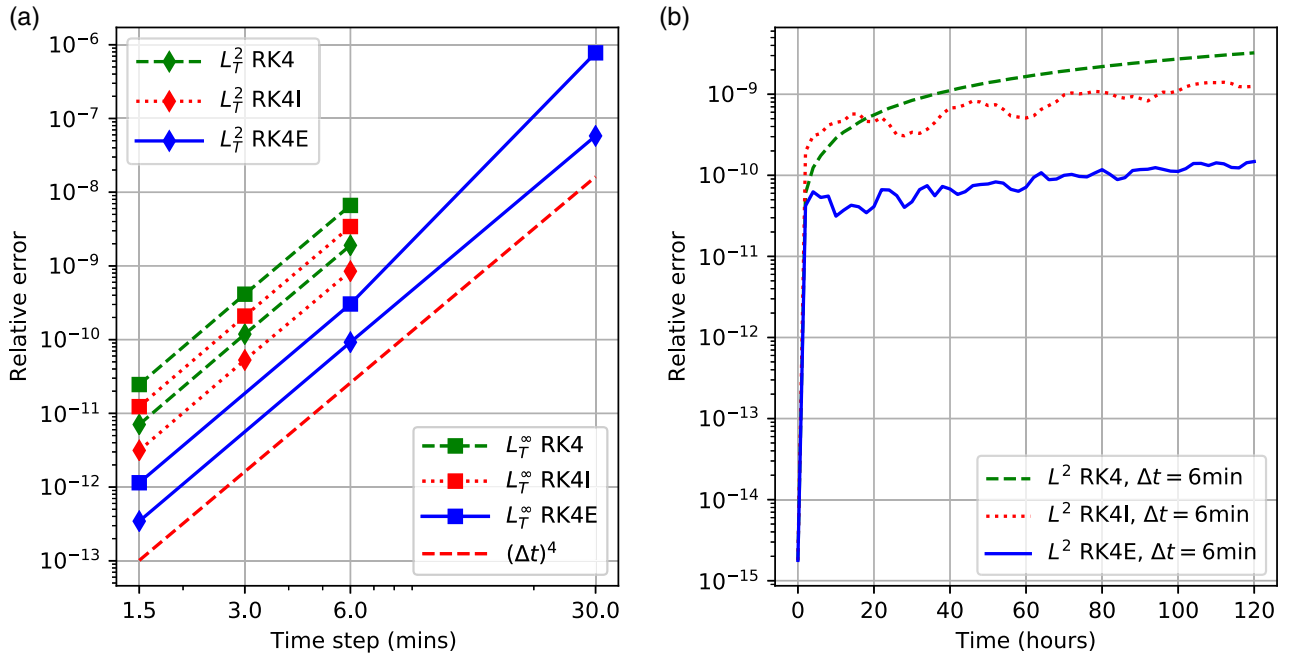


**FIGURE 4** Simulation of solid-body rotation with T42 resolution, comparison of relative error in height field for RK4, RK4E, and RK4I numerical schemes: (a) relative error as a function of time step and (b) error dynamics for $\Delta t = 1.5$ min [Colour figure can be viewed at wileyonlinelibrary.com]

In this test, RK4E extends the usable time-step of RK4 by a factor of 4. The IF scheme improves the accuracy of RK4 by approximately a factor of 2. The accuracy gain is purely due to the elimination of integration errors in the linear part of the spectral equation, as the flow lacks high-frequency components.

## 4.3 | Simulation of barotropic instability

The barotropic instability test for RSW equations was proposed by Galewsky *et al.* (2004). The initial condition for this test is a balanced jet,

$$u = u_0\, b(x)\, b(x_e - x)\, \exp(4.0/x_e), \quad v = 0,$$
$$h = h_0 - \frac{1}{g}\int_{-\pi/2}^{\varphi}\left(2\Omega\sin\varphi' + \frac{u(\varphi')\,\tan\varphi'}{a}\right)u(\varphi')\,d\varphi', \tag{30}$$

where

$$x = x_e(\varphi - \varphi_b)/(\varphi_e - \varphi_b),$$
$$b(x) = \begin{cases} 0 & \text{if } x \le 0, \\ \exp(x^{-1}) & \text{if } x > 0, \end{cases} \tag{31}$$

on top of which is superimposed a localized bell-shaped perturbation in the height field,

$$h' = \tilde{h}\,\cos\varphi\, e^{-(\lambda/\alpha)^2} e^{-[(\varphi_2-\varphi)/\beta]^2}, \tag{32}$$

where $-\pi < \lambda < \pi$. The values of the parameters are $u_0 = 80\,\mathrm{m\cdot s^{-1}}$, $\varphi_b = \pi/7$, $\varphi_e = \pi/2 - \varphi_b$, $h_0 = 10{,}000$ m, while the perturbation is chosen with $\alpha = 1/3$, $\beta = 1/15$, $\varphi_2 = \pi/4$, and $\tilde{h} = 120$ m. As before, the simulation applies no diffusion.

As the instability matures between days 4 and 6, narrow vorticity gradients are developed in the flow (Figure 5). Their simulation requires a fine spatial resolution and represents a challenge to time-stepping schemes in terms of stability and accuracy (Weller, 2014; Scott *et al.*, 2016) . Solutions for RK4E simulations at $T_{42}$, $T_{85}$, and $T_{170}$ resolutions exhibit features typical for spectral models at their respective resolutions (e.g., Galewsky *et al.*, 2004; Scott *et al.*, 2004). An important difference is that the present solutions are obtained with a much greater time step $\Delta t = 24$ min (compared with $\Delta t = 30$ s in Galewsky *et al.* (2004). The T42 solution captures large-scale features of the dynamics, such as the instability release time and overall shape of the vorticity field, including the wavenumber, approximately correct phase, and relatively straight path of the jet through about a quarter of the globe, but fails with regard to details and produces an unrealistic "corrugated hose" vorticity field by day 6. The $T_{85}$ and $T_{170}$ simulations show a progressive improvement in the representation of fine details, as seen in higher resolution inviscid simulations (Weller, 2014).

Figure 6 compares the absolute errors in height and relative vorticity for all the numerical schemes tested at time step $\Delta t = 6$ min. Since there is no analytical solution,

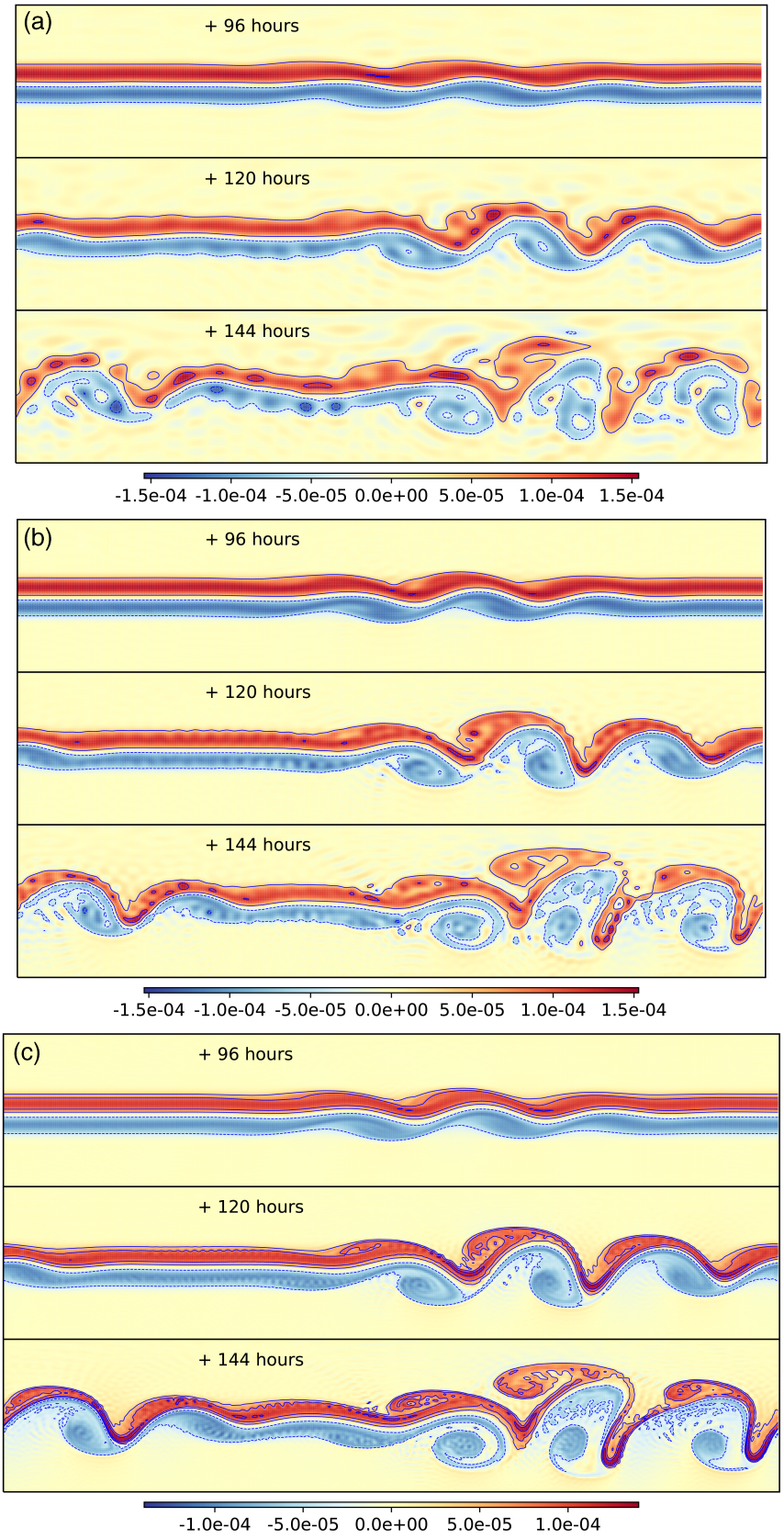


**FIGURE 5** Relative vorticity (in $s^{-1}$) in the barotropic instability test after 4, 5, and 6 days computed with RK4E and $\Delta t = 24$ min. (a) $T_{42}$ resolution, (b) $T_{85}$ resolution, and (c) $T_{170}$ resolution. The three panels in each figure correspond to 96, 120, and 144 hr long simulations (top to bottom). Negative contours are dotted [Colour figure can be viewed at wileyonlinelibrary.com]

the reference must be obtained numerically. In this case, the $T_{85}$ RK4 simulation with 10 times smaller time step $\Delta t = 0.6$ min serves as a reference. The reference solution (plot is not provided) is visually indistinguishable from the one shown in Figure 5b. It transpires that the modified methods are significantly more accurate than the

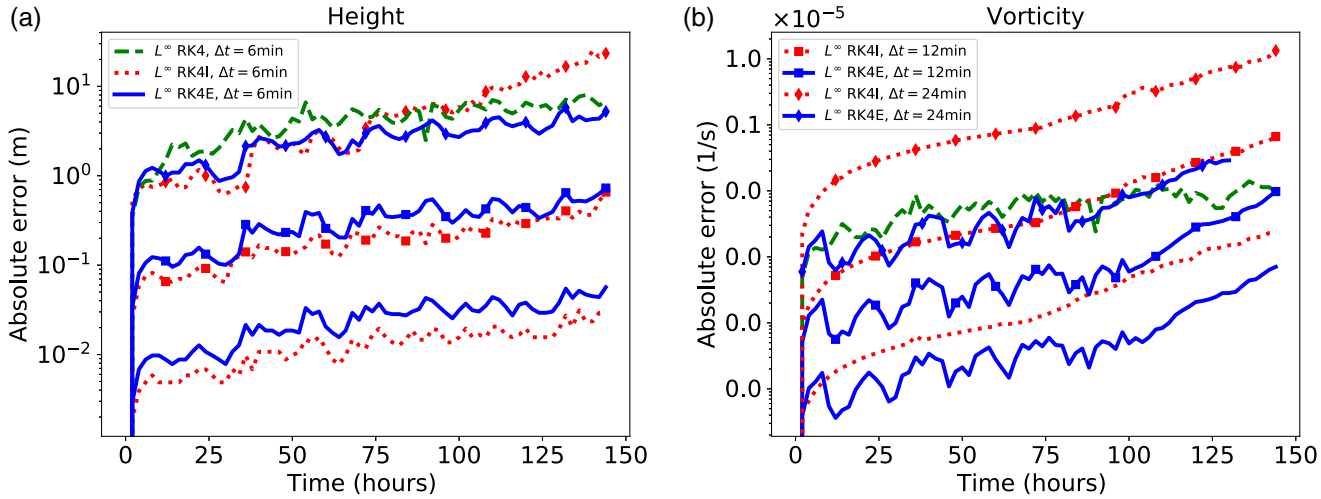


**FIGURE 6** Absolute errors in (a) height and (b) relative vorticity for $T_{85}$ simulations. The reference solution is obtained using RK4 with $\Delta t = 36$ s [Colour figure can be viewed at wileyonlinelibrary.com]

classical RK4. On average, RK4 produces height errors that are approximately 330 and 200 times as large as those of RK4I and RK4E, respectively. In the vorticity field, the pecking order is somewhat different, with the IF method performing worse than the exponential one. Nevertheless, both modified methods significantly outperform the classical Runge–Kutta; on average, RK4E and RK4I respectively yield 150- and 15-fold improvement over RK4. Notably, RK4E with 24-min time-step still performs slightly better than the classical method, with four times smaller time step in height, and matches it in vorticity errors.

Figure 7 provides an efficiency and convergence comparison at $T_{85}$ resolution, further highlighting the benefits of the IF and exponential algorithms. For large time steps, all schemes exhibit order reduction. However, while RK4 reduces to second or third order for larger and smaller time steps, respectively, the ETD and IF schemes perform closer to their classical order.

Increasing the resolution does not change the picture qualitatively. Figure 8 compares $T_{170}$ simulations with $\Delta t = 4$ min. This time we obtained the reference solution using RK4 with 15-s time-step. Quantitatively, compared with $T_{85}$ case, the errors decreased 5–10 times for all schemes. Nevertheless, the accuracy gap between modified methods and RK4 has widened slightly. As before, RK4I is the most accurate in resolving height, while RK4E makes smaller errors in the vorticity field.

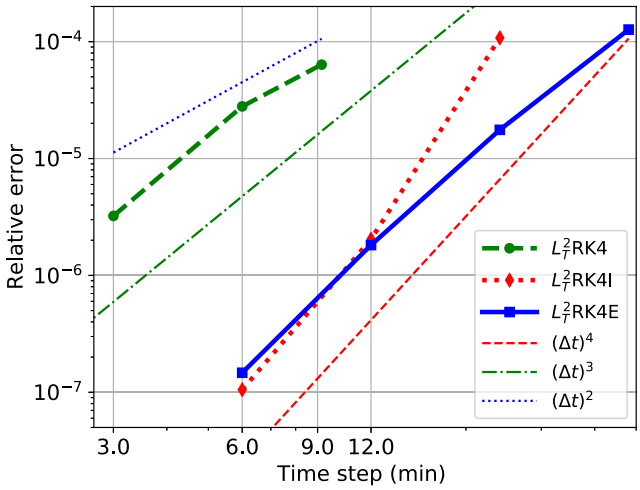


**FIGURE 7** Relative errors in height as a function of time step for barotropic instability test at $T_{85}$ resolution. The reference solution is obtained using RK4 with $\Delta t = 36$ s [Colour figure can be viewed at wileyonlinelibrary.com]

### 4.3.1 | Evaluation of barotropic instability simulation in modal space

The differences in performance of the numerical schemes are now analyzed separately for errors in spectral coefficients corresponding to Rossby and IG modes, a direct output in TIGAR. Figure 9 shows such an analysis for the $T_{170}$ simulation. It is evident that the IF and ETD schemes improve the accuracy of the computation of IG modes by several orders of magnitude (250–500 times) compared with RK4. The IF method yields a slightly bigger gain than the ETD method. However, RK4E shows a comparable improvement in the accuracy of Rossby modes relative to RK4I, making it overall a superior choice.

A major gain in accuracy of the simulation of gravity waves can be further understood by assessing the stability of different time-stepping algorithms for Rossby and IG modes. For practical applications, it is useful to compare their respective critical step $\Delta t_c$, which we define as the

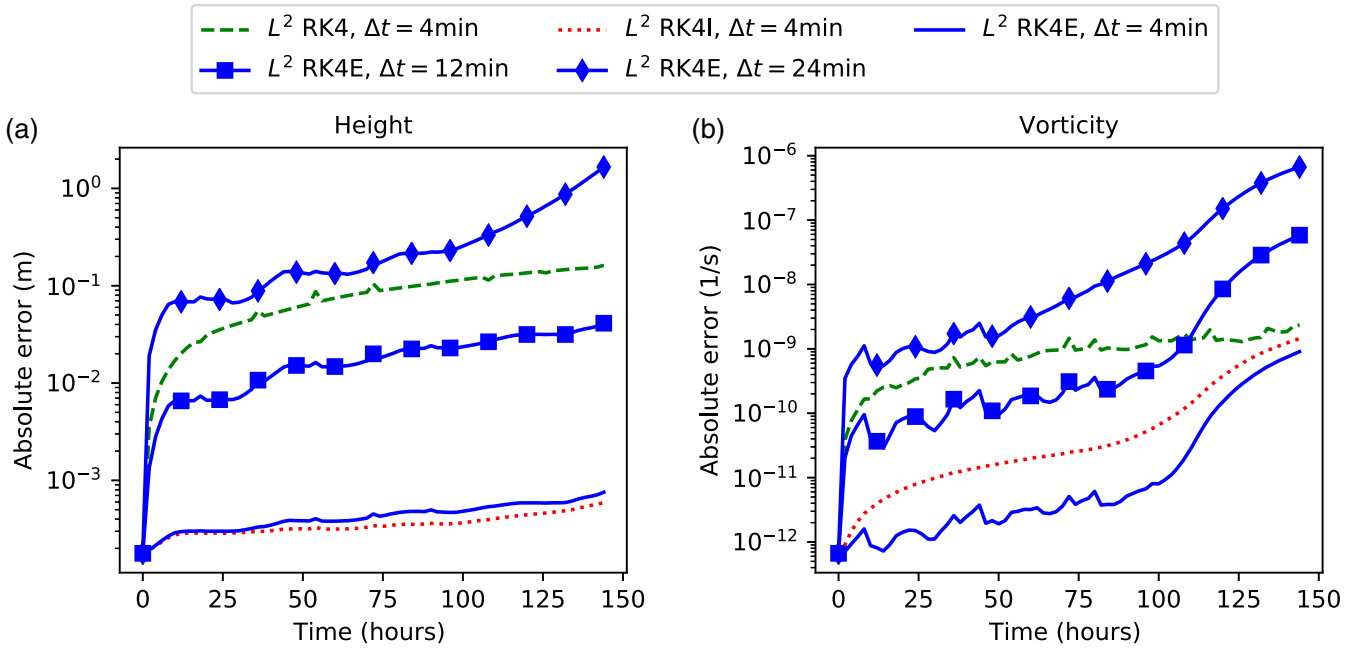


**FIGURE 8** Barotropic instability test, absolute errors in (a) height and (b) relative vorticity for $T_{170}$ simulations. The reference solution is obtained with RK4 using $\Delta t = 15$ s [Colour figure can be viewed at wileyonlinelibrary.com]

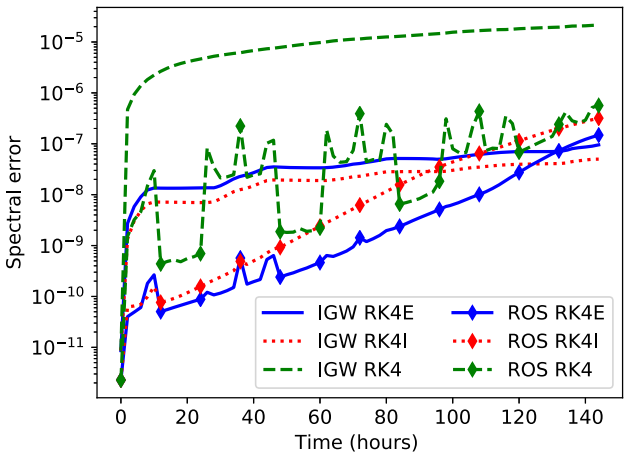


**FIGURE 9** Barotropic instability test, $T_{170}$ with $\Delta t = 4$ min. Errors in Hough spectral coefficients corresponding to Rossby and inertia–gravity modes. $\ell^2$ norms are plotted, with zonal wavenumber $k = 0$ modes excluded [Colour figure can be viewed at wileyonlinelibrary.com]

largest time step with which the six-day diffusion-free simulation can be completed without blowing up. In order to understand the mechanism behind the stability gains associated with RK4E better, we also perform the barotropic instability test on hybrid spectral grids $T_{170/85}$ and $T_{170/42}$, where the resolved IG modes are identical to $T_{170}$ resolution, whereas the resolved Rossby modes correspond to $T_{85}$ and $T_{42}$ resolutions, respectively. The spatial grid in both cases is the 512×256 Gaussian grid, optimal for the $T_{170}$ resolution.

**TABLE 1** Critical time steps in minutes for barotropic instability test

| Method | RK4 | RK4I | RK4E |
|---|---|---|---|
| $T_{42}$ | 19.5 | 48.0 | 144.0 |
| $T_{85}$ | 9.2 | 24.0 | 51.4 |
| $T_{170}$ | 4.6 | 10.9 | 24.0 |
| $T_{170/85}$ | 4.6 | | 40.0 |
| $T_{170/42}$ | 4.6 | | 130.9 |

*Note:* $T_{170/85}$ and $T_{170/42}$ are spectral grids with IG modes identical to $T_{170}$ and Rossby modes identical to $T_{85}$ and $T_{42}$, respectively.

The results are summarized in Table 1. We remark that the numbers in Table 1 are close to the worst-case scenario for the respective methods. Simpler multiscale flows, such as the geostrophic adjustment experiment, can be simulated with a time step several times larger. For the classical RK scheme, the critical time step on both hybrid grids is identical with that of $T_{170}$, fully in accord with the idea that the stability of a classical scheme is limited by fast gravity wave dynamics. This, however, is in stark contrast to the exponential time-stepping, where the critical time steps for $T_{170/85}$ and $T_{170/42}$ closely match those of $T_{85}$ and $T_{42}$, respectively, which indicates that the stability of RK4E is determined by the Rossby component of the flow. Such a conclusion is further confirmed by studying the blow-up dynamics for time steps that exceed $\Delta t_c$.

This phenomenon can be explained as follows. The only source of instability in the ETD scheme is wave–wave

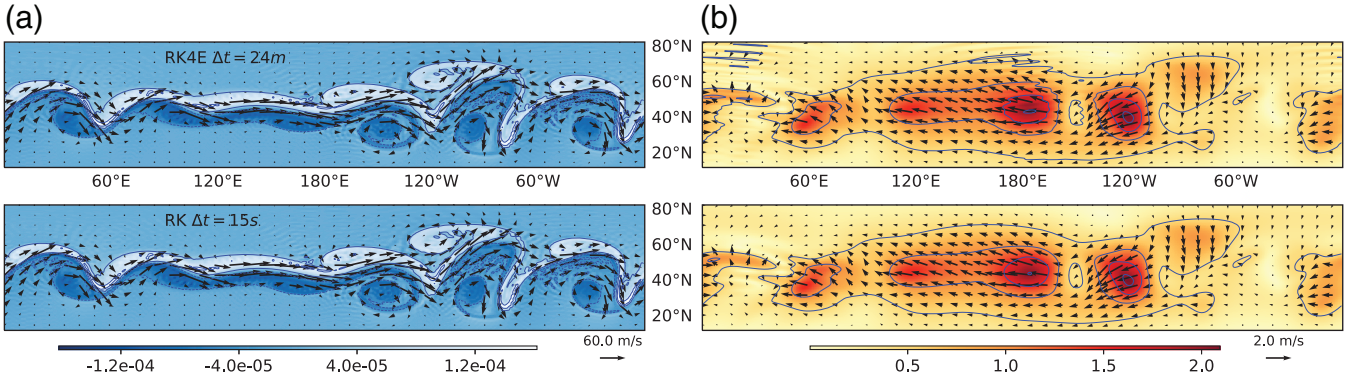


**FIGURE 10** Winds simulated in $T_{170}$ barotropic instability test after 144 hours, separated into (a) Rossby and (b) IG modes. (a) Relative vorticity (shades and contours, in $s^{-1}$) and horizontal wind vectors of Rossby modes, (b) horizontal wind vectors and wind speed (shades and contours) in IG modes. The top panels correspond to RK4E with $\Delta t = 24$ min, and the bottom panels show the referent RK4 solution with $\Delta t = 15$ s. Negative contours are dotted [Colour figure can be viewed at wileyonlinelibrary.com]

interactions. Analyzing the structure of nonlinear terms in Equation 16, it is clear that triggering unbounded growth requires formation of large velocity and/or height gradients in the flow, which is often referred to as an enstrophy cascade to small scales. The contribution of IG waves to the large vorticity gradients is of transient nature, due to large propagation speed of gravity waves compared with Rossby waves. A high stiff-order numerical scheme such as RK4E is capable to recover successfully from temporary growth originating in IG modes, thanks to its large stability domains and slow error build-up. In contrast, when the gradients originate in Rossby modes, they persist for a longer time due to the slow propagation speed of Rossby waves, eventually leading to a blow-up.

It is important to stress that the stability increase for IF and ETD schemes comes through a better representation of gravity waves, which leads to a greater accuracy, rather than through damping of small scales. Figure 10 compares the Rossby and IG components of the flow from the RK4E simulation with $\Delta t$ =24 min and the reference solution computed with RK4 and 96 times finer time step. It shows that the amplitudes of the IG modes are much smaller than the Rossby mode amplitudes. Some small-scale differences between the two simulations can be noticed for the gravity component, but the two solutions are overall remarkably similar for the chosen time step and forecast length. For the presented snapshot, the bulk of gravity-wave activity is located in the jet core region, thus rendering the comparison representative.

Finally, we compare energy spectra in Rossby and IG modes in RKE and RK4 forecasts (Figure 11). Energy in TIGAR encompasses both kinetic energy and available potential energy and is easily computed from the Hough expansion coefficients as

$$E_l = \frac{1}{2} g D \sum_k \sum_n W^k_{n,l} \left[ W^k_{n,l} \right]^*, \quad \text{colours} \tag{33}$$

where $l$ takes values 1 and 2 for EIG and WIG modes, respectively, whereas $l = 3$ provides energy associated with Rossby modes. The sum of total energy computed by Equation 33 for $l = 1, 2, 3$ is equal to the globally integrated kinetic energy (in $J \cdot kg^{-1}$) and the potential energy, defined as $g/D\, h^2$ (Kasahara and Puri, 1981).

Figure 11a shows that the Rossby wave energy increases over time at the expense of the mean flow. Instability leads to the generation of IG waves, but their energy remains well below 1% until the end of simulation. The comparison of reference energy spectra for Rossby and IG modes with RK4E solutions for 48 and 96 times greater time steps is shown after 3, 5, and 6 days of simulations (Figure 11b–d). It shows that RK4E resolves the Rossby spectrum already with the largest stable step size for this simulation, $\Delta t = 24$ min. The gravity wave spectrum is also mostly resolved at $\Delta t = 24$ min, except for the growing instability in zonal wavenumbers 60–100. Reducing the step size to 12 min results in a fully reproduced gravity wave spectrum at all wavenumbers.

## 4.4 | Summary of the comparison of time-stepping schemes

The three schemes presented show the accuracy befitting a fourth-order method. Nevertheless, the use of IF and ETD in TIGAR leads to remarkable gains in both accuracy/efficiency and stability compared with the already

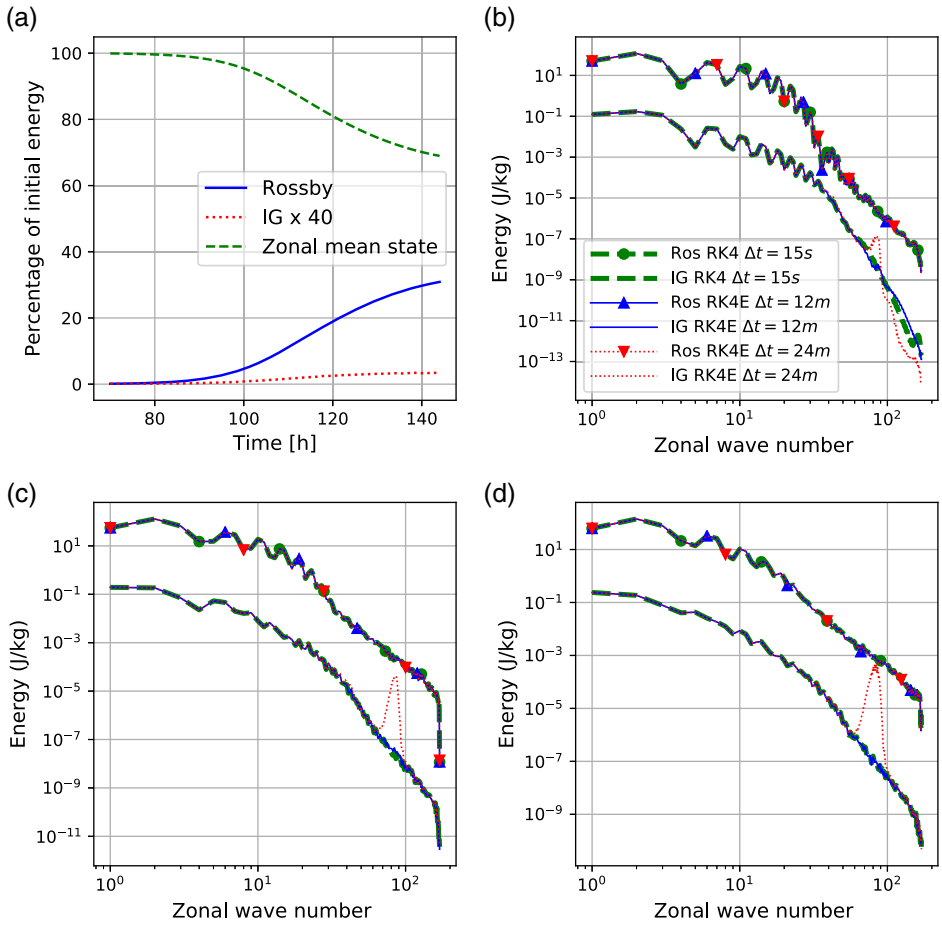


**FIGURE 11** (a) Evolution of total energy in the referent $T_{170}$ barotropic instability simulation RK4 with $\Delta t = 15$ s. Energy spectra of Rossby and IG modes after (b) 72, (c) 120, and (d) 144 hr. In each case, the referent solution is compared with RK4E results for 12- and 24-min time steps [Colour figure can be viewed at wileyonlinelibrary.com]

well-performing RK4. These gains clearly manifest themselves already in simple flows such as steady-state or rotating solutions. However, much more relevant is performance in multiscale flows, here represented by barotropic instability. In a multiscale setting, the gains are significantly larger, as stiffness of the spectral ODE starts to play a significant role. The findings can be summarized as follows.

- **Stability:** The exponential method allows for 5–6 times larger time step than RK4. The integrating factor method yields approximately 2.5-fold increase in stability in this setting.
- **Efficiency:** Both RK4I and RK4E provide 2–3 orders better accuracy than RK4 for the same amount of work. RK4E is clearly the best choice at large step sizes, with RK4I becoming competitive with it at moderate to small $\Delta t$.
- **IF versus ETD versus classical schemes:** The differences between the algorithms of different types are best understood in terms of their effect on spectral coefficients. Both IF and ETD schemes are vastly superior to the stem RK4 in resolving gravity modes, improving the accuracy of the corresponding spectral coefficients by several orders of magnitude. The IF method is the best in this regard, but the exponential scheme is not too far behind. However, the ETD method also provides large gains in Rossby modes, while for RK4I the gains here are smaller. Since Rossby modes dominate in the atmosphere, this makes ETD methods a better choice for NWP systems.

In our testing, the fourth-order exponential method RK4E due to Cox and Matthews (2002) has emerged as clearly the best scheme. The method shows no apparent weaknesses and is the top performer in all three key categories: stability, efficiency, and accuracy. The IF method can match the performance of RK4E under particular conditions. In barotropic instability tests, RK4E allows for time steps six times as large as the classical method and matches the accuracy of RK4 with approximately four times larger time step. Thus, using high-order ETD schemes with large time steps in the Hough framework enables high-precision forecasts at moderate computational expense. We notice that a similar conclusion on the practicality of high-order ETD schemes was reached by Kassam and Trefethen (2005).

## 5 | CONCLUSIONS AND OUTLOOK

Motivated by the need to evaluate nonlinear terms in primitive equations accurately and to forecast gravity wave dynamics, we developed a new global prognostic model dynamical core based on the Hough harmonics as basis functions. The feasibility of such a model was demonstrated by Kasahara (1977; 1978) but, despite obvious benefits and a few attempts in the past (Callaghan *et al.*, 1999), Hough harmonics based models did not gain popularity. The work presented here reintroduces such a model under the acronym Transient Inertia–Gravity And Rossby wave dynamics model (TIGAR). We describe the horizontal component of the model, which solves the nonlinear rotating shallow-water equations on the sphere, and present model performance for several well-known tests. High-precision computations are achieved through the use of higher order integrating factor and exponential time-differencing methods, enabled by the normal mode framework, which address stability issues associated with gravity wave dynamics.

The results demonstrate numerical benefits of the Hough harmonics basis. By construction, the Hough spectral model is an ODE in the normal form, where the linear part is given by a diagonal matrix. This structure leads to a tremendous increase in efficiency of integrating factor and exponential time-differencing schemes. These schemes are known to be remarkably stable and accurate for stiff systems, but are generally expensive, due to the cost of evaluating the matrix exponential. This drawback, however, completely disappears for the system in the normal form, thus making a combination of the Hough model and exponential time-stepping very attractive indeed.

Barotropic instability simulations show that TIGAR is capable of resolving complex multiscale flows with high accuracy. For example, simulations with a mean depth of 10 km after a week of integration produce errors in the geopotential height field that typically do not exceed several centimeters. Among different methods tested, the fourth-order exponential Runge–Kutta method first studied by Cox and Matthews (2002) performed the best. It leads to an approximately sixfold increase in the CFL time-step bound on multiscale flows, compared with the almost equally expensive RK4. Importantly, the stability gains are achieved through improvements in the gravity wave resolution, rather than through damping of high-frequency modes, resulting in enhanced accuracy and efficiency. The accuracy is increased by a factor of 50–100, when used with an equal time step, or the computational time is decreased four times, while matching the RK4 accuracy, when a proportionally larger time step is chosen. There is a potential for further improvement of the fourth-order exponential Runge–Kutta method. For example, Krogstad (2005) proposed an ETD modification of RK4, which has stiff order 3 as opposed to 2 for the Cox and Matthews (2002) method. Exponential schemes can be combined with split time-stepping algorithms, leading to yet better resolution of the gravity wave dynamics.

All the simulations presented in this work use no explicit damping. The ability to run the model without numerical damping is beneficial, as it allows simulations with dissipation representing physical processes only. We speculate that weakening of numerical dissipation can lead to improvement in energy balances, wave–wave interactions, and variability in the numerical models.

Potential advantages of the Hough harmonics framework extend far beyond the time-stepping options. Compared with traditional spectral models utilizing spherical harmonics, the normal-mode function formulation comes bundled with additional structure containing useful information such as a diagonal linear propagator, eigenfrequencies of its components, and linear mass–wind balance. This facilitates research of their roles in physical processes, data assimilation, and predictability, with a bearing on many aspects of weather and climate models. In particular, the ease with which physically motivated selective filtering can be implemented in a model based on Hough harmonics is of great benefit to research. Reduced models such as the quasigeostrophic model or the tropical wave model can be obtained with relatively trivial changes in the model configuration.

## ACKNOWLEDGEMENTS

It is a pleasure to acknowledge discussions with Dr Akira Kasahara, who pioneered the application of Hough harmonics as basis functions of a forecast model, and with our colleagues Richard Blender and Frank Lunkeit. We are indebted to Dr Nils Wedi and an anonymous reviewer for their valuable comments, which led to an improved presentation, and to Ms Wenlin Xiao for drawing Figure 1.

Open Access funding enabled and organized by Projekt DEAL.

## ORCID

*Sergiy Vasylkevych* https://orcid.org/0000-0003-1878-1979

*Nedjeljka Žagar* https://orcid.org/0000-0002-7256-5073

## REFERENCES

Andrews, D.G., Holton, J.R. and Leovy, C.B. (1987) *Middle Atmosphere Dynamics*. San Diego: Academic Press, Inc.

Benacchio, T. and Klein, R. (2019) A semi-implicit compressible model for atmospheric flows with seamless access to soundproof and hydrostatic dynamics. *Monthly Weather Review*, 147, 4221–4240.

Berland, H., Owren, B. and Skaflestad, B. (2006) Solving the nonlinear Schrödinger equation using exponential integrators. *Modelling, Identification and Control*, 27, 201–217.

Boyd, J.P. (2001) *Chebyshev and Fourier Spectral Methods*, Vol. 2001. Mineola, NY: Dover.

Boyd, J.P. (2018) *Dynamics of the Equatorial Ocean*. Berlin: Springer-Verlag GmbH.

Browning, G.L., Hack, J.J. and Swarztrauber, P.N. (1989) Accuracy of rotational and divergent kinetic energy spectra diagnosed from flight/track winds. *Monthly Weather Review*, 117, 1058–1075.

Callaghan, P., Fusco, A., Francis, G. and Salby, M. (1999) A Hough spectral model for three-dimensional studies of the middle atmosphere. *Journal of the Atmospheric Sciences*, 56, 1461–1480.

Certaine, J. (1960) The solution of ordinary differential equations with large time constants. In: *Mathematical Methods for Digital Computers*, New York, NY: Wiley, pp. 128–132.

Clancy, C. and Pudykiewicz, J.A. (2013) On the use of exponential time integration methods. *Tellus A*, 65, 20898.

Coudiére, Y., Douanla-Lontsi, C. and Pierre, C. (2018) Exponential Adams–Bashforth integrators for stiff ODEs, application to cardiac electrophysiology. *Mathematics and Computers in Simulation*, 153, 15–34.

Cox, S.M. and Matthews, P.C. (2002) Exponential time differencing for stiff systems. *Journal of Computational Physics*, 176, 430–455.

Dee, D.P. and Da Silva, A.M. (1986) Using Hough harmonics to validate and assess nonlinear shallow-water models. *Monthly Weather Review*, 114, 2191–2196.

Dörnbrack, A., Gisinger, S., Kaifler, N., Portele, T., Bramberger, M., Rapp, M., Gerding, M., Söder, J., Žagar, N. and Jelić, D. (2018) Gravity waves excited during a minor sudden stratospheric warming. *Atmospheric Chemistry and Physics*, 18, 12915–12931.

Errico, R.M. (1997) On the removal of gravitational noise in numerical forecasts. *Journal of the Meteorological Society of Japan*, 75, 219–227.

Flattery, T. W. (1971) Spectral models for global analysis and forecasting. In Technical Report 242, Automated Weather Support: Proceedings of the 6th AWS Technical Exchange Conference, U.S. Naval Academy, 21-24 September 1970, Air Weather Service (MAC), pp. 42–54.

Fraedrich, K., Kirk, E. and Lunkeit, F. (2009) *Puma Portable University Model of the Atmosphere*. Hamburg: World Data Center for Climate (WDCC) at DKRZ.

Galewsky, J., Scott, R.K. and Polvani, L.M. (2004) An initial-value problem for testing numerical models of the global shallow-water equations. *Tellus A: Dynamic Meteorology and Oceanography*, 56, 429–440.

Gaudreault, S. and Pudykiewicz, J.A. (2016) An efficient exponential time integration method for the numerical solution of the shallow water equations on the sphere. *Journal of Computational Physics*, 322, 827–848.

Gelb, A. and Gleeson, J. (2001) Spectral viscosity for shallow water equations in spherical geometry. *Monthly Weather Review*, 129, 2346.

Hochbruck, M. and Ostermann, A. (2010) Exponential integrators. *Acta Numerica*, 19, 209–286.

Hoskins, B.J. and Simmons, A.J. (1988) A multi-layer spectral model and the semi-implicit method. *Quarterly Journal of the Royal Meteorological Society*, 116, 1587–1598.

Kasahara, A. (1977) Numerical integration of the global barotropic primitve equations with Hough harmonic expansions. *Journal of the Atmospheric Sciences*, 34, 687–701.

Kasahara, A. (1978) Further studies on a spectral model of the global barotropic primitve equations with Hough harmonic expansions. *Journal of the Atmospheric Sciences*, 35, 2043–2051.

Kasahara, A. (2020) 3D Normal mode functions (NMFs) of a global baroclinic atmospheric model. In N. Žagar and J. Tribbia (Eds.), *Modal View Of Atmospheric Variability: Applications Of Normal-Mode Function Decomposition in Weather and Climate Research. Mathematics of Planet Earth Series* Vol. 8, Cham: Springer, pp. 1–62.

Kasahara, A. and Puri, K. (1981) Spectral representation of three-dimensional global data by expansion in normal mode functions. *Monthly Weather Review*, 109, 37–51.

Kassam, A.-K. and Trefethen, L.N. (2005) Fourth-order time-stepping for stiff PDEs. *SIAM Journal on Scientific Computing*, 26, 1214–1233.

Kitamura, Y. and Matsuda, Y. (2010) Energy cascade processes in rotating stratified turbulence with application to the atmospheric mesoscale. *Geophysical Research Letters*, 115, L11104. https://doi.org/10.1029/2009JD012368.3013-3030.

Ko, S.D., Tribbia, J.J. and Boyd, J.P. (1981) Energetics analysis of a multilevel global spectral model. Part I: Balanced energy and transient energy. *Monthly Weather Review*, 117, 1941–1953.

Krogstad, S. (2005) Generalized integrating factor methods for stiff PDEs. *Journal of Computational Physics*, 203, 72–88.

Läuter, M., Handorf, D. and Dethloff, K. (2005) Unsteady analytical solutions of the spherical shallow water equations. *Journal of Computational Physics*, 210, 535–553.

Lawson, D.J. (1967) Generalized Runge–Kutta processes for stable systems with large Lipschitz constants. *SIAM Journal on Numerical Analysis*, 4, 372–380.

Longuet-Higgins, M.S. (1968) The eigenfunctions of Laplace's tidal equations over a sphere. *Philosophical Transactions of the Royal Society of London, Series A. Mathematical and Physical Sciences*, 262, 511–607.

Matsuno, T. (1966) Quasi-geostrophic motions in the equatorial area. *Journal of the Meteorological Society of Japan*, 44, 25–42.

Mengaldo, G., Wyszogrodzki, A., Diamantakis, M., Lock, S.-J., Giraldo, F.X. and Wedi, N.P. (2019) Current and emerging time-integration strategies in global numerical weather and climate prediction. *Archives of Computational Methods in Engineering*, 26, 663–684.

Minchev, B. and Wright, W. (2005) *A review of exponential integrators for first order semilinear problems*. Trondheim, Norway: Department of Mathematical Sciences, Norwegian University of Science and Technology. Technical Report 2/2005.

Nørsett, S.P. (1969) An a-stable modification of the Adams–Bashforth methods. In: *Conference on Numerical Solution of Differential Equations (Dundee, 1969)*, Berlin: Springer, pp. 214–219.

Palmer, T. and Stevens, B. (2019) The scientific challenge of understanding and estimating climate change. *Proceedings of the National Academy of Sciences*, 116, 24390–24395.

Peixoto, P.S. and Schreiber, M. (2019) Semi - Lagrangian exponential integration with application to the rotating shallow water equations. *SIAM Journal on Scientific Computing*, 41, B903–B928.

Plougonven, R. and Zhang, F. (2014) Internal gravity waves from atmospheric jets and fronts. *Reviews of Geophysics*, 52, 33–76.

Ritchie, H. (1988) Application of the semi - Lagrangian method to a spectral model of the shallow water equations. *Monthly Weather Review*, 116, 1578–1598.

Satoh, M. (2013) *Atmospheric Circulation Dynamics and General Circulation Models*. 2nd edition, Berlin, Heidelberg: Springer-PRAXIS.

Scott, R.K., Harris, L.M. and Polvani, L.M. (2016) A test case for the inviscid shallow-water equations on the sphere. *Quarterly Journal of the Royal Meteorological Society*, 142, 488–495, https://rmets.onlinelibrary.wiley.com/doi/abs/10.1002/qj.2667.

Scott, R.K., Rivier, L., Loft, R. and Polvani, L.M. (2004) *Bob: Model description and user's guide. No. NCAR/TN-456+IA*. Boulder: University Corporation for Atmospheric Research. https://opensky.ucar.edu/islandora/object/technotes%3A462

Shigehisa, Y. (1983) Normal modes of the shallow water equations for zonal wavenumber zero. *Journal of the Meteorological Society of Japan*, 61, 479–493.

Smolarkiewicz, P.K., Kühnlein, C. and Wedi, N.P. (2019) Semi-implicit integrations of perturbation equations for all-scale atmospheric dynamics. *Journal of Computational Physics*, 376, 145–159.

Swarztrauber, P.N. (1981) The approximation of vector functions and their derivatives on the sphere. *SIAM Journal on Numerical Analysis*, 18, 191–210.

Swarztrauber, P.N. and Kasahara, A. (1985) The vector harmonic analysis of Laplace tidal equations. *SIAM Journal on Scientific and Statistical Computing*, 6, 464–491.

Tanaka, H. and Kasahara, A. (1992) On the normal modes of Laplace's tidal equations for zonal wavenumber zero. *Tellus A*, 44, 18–32.

Tanaka, H. and Žagar, N. (2020) 3D modal variability and energy transformations on the sphere. In: N. Žagar and J. Tribbia (Eds.), *Modal View Of Atmospheric Variability: Applications Of Normal-Mode Function Decomposition in Weather and Climate Research, Mathematics of Planet Earth Series* Vol. 8, Cham: Springer, pp. 121–179.

Temperton, C. (1991) On scalar and vector transform methods for global spectral models. *Monthly Weather Review*, 119, 1303–1307.

Terasaki, K., Tanaka, H. and Žagar, N. (2011) Energy spectra of Rossby and gravity waves. *SOLA*, 11, 45–48.

Tokman, M. (2006) Efficient integration of large stiff systems of ODEs with exponential propagation iterative (EPI) methods. *Journal of Computational Physics*, 213, 748–776.

Tribbia, J. (1984) A simple scheme for high-order nonlinear normal mode initialization. *Monthly Weather Review*, 112, 278–284.

Žagar, N., Anderson, J.L., Collins, N., Hoar, T., Raeder, K., Lei, L. and Tribbia, J. (2016a) Scale-dependent representation of the information content of observations in the global ensemble Kalman filter data assimilation. *Monthly Weather Review*, 144, 2927–2945.

Žagar, N., Blaauw, M., Jesenko, B. and Magnusson, L. (2016b) Diagnosing model performance in the Tropics. *ECMWF Newsletter*, 147, 26–33, http://www.ecmwf.int/publications/newsletters.

Žagar, N., Buizza, R. and Tribbia, J. (2015a) A three-dimensional multivariate modal analysis of atmospheric predictability with application to the ECMWF ensemble. *Journal of the Atmospheric Sciences*, 72, 4423–4444.

Žagar, N., Jelić, D., Blaauw, M. and Bechtold, P. (2017) Energy spectra and inertia–gravity waves in global analyses. *Journal of the Atmospheric Sciences*, 74, 2447–2466.

Žagar, N., Kasahara, A., Terasaki, K., Tribbia, J. and Tanaka, H. (2015b) Normal-mode function representation of global 3D datasets: open-access software for the atmospheric research community. *Geoscientific Model Development*, 8, 1169–1195.

Žagar, N. and Tribbia, J.E. (2020) *Modal View of Atmospheric Variability: Applications of Normal-Mode Function Decomposition in Weather and Climate Research. Mathematics of Planet Earth Series* Vol. 8. Cham: Springer Nature.

Wang, H., Boyd, J. and Akmaev, R. (2016) On computation of Hough functions. *Geoscientific Model Development*, 9, 1477–1488.

Wedi, N.P., Polichtchouk, I., Dueben, P., Anantharaj, V.G., Bauer, P., Boussetta, S., Browne, P., Deconinck, W., Gaudin, W., Hadade, I., Hatfield, S., Iffrig, O., Lopez, P., Maciel, P., Mueller, A., Saarinen, S., Sandu, I., Quintino, T. and Vitart, F. (2020) A baseline for global weather and climate simulations at 1 km resolution. *Journal of Advances in Modeling Earth Systems*, 12, e2020MS002192.

Weller, H. (2014) Non-orthogonal version of the arbitrary polygonal C-grid and a new diamond grid. *Geoscientific Model Development*, 7, 779–797.

Williamson, D.L., Drake, J.B., Hack, J.J., Jakob, R. and Swarztrauber, P.N. (1992) A standard test set for numerical approximations to the shallow water equations in spherical Geometry. *Journal of Computational Physics*, 102, 211–224.

**How to cite this article:** Vasylkevych S, Žagar N. A high-accuracy global prognostic model for the simulation of Rossby and gravity wave dynamics. *Q.J.R. Meteorol. Soc*. 2021;147:1989–2007. https://doi.org/10.1002/qj.4006